Research Square

Preprints are preliminary reports that have not undergone peer review.
They should not be considered conclusive, used to inform clinical practice,
or referenced by the media as validated information.

Hybrid bias field correction scheme driving inhomogeneous image segmentation

Baoli Shi

blshi213@henu.edu.cn

Henan

Xingru Jiang

Henan

Shuhong Zhang

Henan

Research Article

Keywords:

Posted Date: November 26th, 2026

DOI: https://doi.org/10.21203/rs.3.rs-11609331/v1

License: This work is licensed under a Creative Commons Attribution 4.0 International License.
Read Full License

Additional Declarations: No competing interests reported.

Noname manuscript No.
(will be inserted by the editor)

Hybrid bias field correction scheme driving inhomogeneous image segmentation

Baoli Shi*, Xingru Jiang and Shuhong Zhang

the date of receipt and acceptance should be inserted later

Abstract Intensity inhomogeneity degrades segmentation quality by reducing the contrast between target and background regions. This paper introduces a segmentation method by using both multiplicative and additive bias fields to correct intensity inhomogeneity, where a soft constraint is imposed on the additive bias field for effective regulation. Especially, the proposed model introduces a Sobolev-type functional space to constrain the smoothness of the bias field and incorporates an edge detection function to enhance adaptability to inhomogeneous regions, thereby effectively suppressing bias field interference while preserving image structure. In order to overcome the nonsmooth of the proposed model, we use the iterative convolution–thresholding method (ICTM) to approximate the total variation term and then use the alternating direction method to solve it. Furthermore, we analyze the mathematical properties of the established model and the proposed method. Numerical experiments on publicly available natural and medical image datasets the proposed model exhibits excellent performance in segmentation accuracy, robustness, and sensitivity to initial contours with comparisons made against several state-of-the-art models.

Keywords Intensity inhomogeneity image segmentation; Multiplicative bias field; Additive bias field; Alternating direction method (ADM)

1 Introduction

Image segmentation constitutes one of the most fundamental tasks in image processing [1–3]. This technique aims to partition digital images into contiguous regions of interest (ROI) that exhibit homogeneous characteristics with respect to intensity, texture, or color features [4,5]. However, current segmentation methods face significant challenges due to inherent limitations in imaging equipment and environmental conditions during acquisition [6,7]. For instance, in natural scene images, intensity inhomogeneities caused by non-uniform illumination and degradation artifacts frequently lead to overlapping intensity distributions across different regions[8,9]. Similarly, in magnetic resonance imaging (MRI), artifacts arising from magnetic field inhomogeneities and boundary discontinuities substantially compromise segmentation accuracy. These technical limitations present considerable obstacles for achieving precise and reliable image segmentation.

Over the past few decades, extensive research has been conducted on image segmentation. In addition to conventional approaches [10,11], various advanced techniques have been emerged, including deep learning-based methods [12–15] and improved variational partial differential equation (PDE) models along with their derivatives [16–19]. Although deep neural networks demonstrate remarkable capabilities in learning and feature extraction—enabling precise segmentation of complex scenes and pixel-level targets—their practical application faces significant limitations. These include poor interpretability, weak generalization, and stringent demands on the volume of training data, network architecture design, and computational resources [20,21]. Given the inherent

School of Mathematics and Statistics, Henan University, Kaifeng, 475000, China. E-mail: blshi213@henu.edu.cn; shibaoli1983@163.com (*corresponding author); jiangxingru@henu.edu.cn; zhangshuhong198@163.com

challenges in image segmentation, no single method can effectively address all difficulties. Consequently, hybrid approaches that integrate deep learning with traditional techniques have gained increasing attention [22–24]. This trend highlights the enduring relevance of conventional methods, which remain indispensable complements to data-driven approaches.

In the evolution of traditional segmentation methods, gradient-based models—particularly those leveraging edge information—have been widely employed. A seminal contribution in this domain is the Active Contour Model (ACM) [25,49], which operates through the interplay of internal and external forces. The internal force acts as a regularization term, maintaining contour smoothness during evolution, while the external force, derived from image features, drives the contour toward the target boundary until convergence. Depending on their representation, the ACM can be classified into explicit and implicit formulations. The parametric representations used in explicit active contour models impose significant topological constraints [27], including the inability to accommodate object splitting and merging during evolution. These limitations severely restrict their application to real-world image segmentation tasks involving topological changes or unknown initial configurations. In contrast, implicit models employ the Level Set Function (LSF) [28] to represent contours, offering greater flexibility in handling complex topologies and irregular shapes without requiring manual initialization. Furthermore, the implicit framework naturally accommodates contour splitting and merging through zero-level set evolution. The variational level set method [29] extends this paradigm by embedding prior knowledge into energy functionals, leading to two primary formulations: Edge-based models [30,31] and Region-based models [32,33]. For edge-based model, they rely on gradient information for boundary detection but struggle with weak edges and noise sensitivity. To the region-based models, they utilize regional descriptors to partition images, rendering them robust to noise and capable of segmenting weakly bounded structures. While region-based methods overcome some limitations of edge-based approaches, they exhibit drawbacks in scenarios with intensity inhomogeneity or faint boundaries, often resulting in slow convergence and suboptimal segmentation accuracy.

To segment the image with intensity inhomogeneity, the addition of local region energy into the model [34–36] is suggested to enhance the performance of region-based level set methods on non-uniform intensity image, taking the Local area-Binary Fit (LBF) model suggested by Li et al. [35] as an illustration. In order to extract the local intensity mean information from the image, the LBF model used two continuous fitting functions and introduced a kernel function to the active contour model. However, this model is more sensitive to the initial profile and tends to converge to a local minimum. On this basis, the bias field estimation formula is further integrated into the level set framework to achieve both bias field correction and image segmentation [37–39], and this class of methods is currently a more popular method, such as the Local Intensity Clustering (LIC) model [37], which considered a multiplicative model of intensity inhomogeneity, used local K-mean clustering and introduced a bias field in the segmentation model to complete the bias field correction, which in turn improved the model dependence on the initial contours. However, the LIC model is not robust to the images with varying degrees of grayscale heterogeneity and noise. In addition, some methods considered additive models of images with intensity inhomogeneities [40–42], and Chan and Vese proposed a segmented smoothing model (PS) [40]. This method used a segmented smoothing function instead of a constant value function to effectively segment images with intensity inhomogeneities. However, the model required periodic initialization when using the level-set method, which is difficult to apply and cannot be generalized. Not only that, but due to the nonconvexity of the model, the solution is prone to fall into local minima. There are also methods of segmenting grayscale inhomogeneous images based on retinal theory, where the perceived intensity of an object is considered as a combination of reflectance and illumination [43–45]. Nevertheless, the utility of these segmentation approaches is predominantly restricted to Retinex-processed natural images and exhibits poor generalizability when applying to medical imaging domains. The primary constraint originates from the chosen function spaces, which insufficiently characterize the mathematical properties of both smooth and piecewise constant anatomical structures in medical images, consequently diminishing segmentation performance.

Recent advances in image segmentation have focused on mitigating intensity inhomogeneity effects by employing composite models that jointly address additive and multiplicative inhomogeneity components [46–49]. Although these approaches improve model flexibility and strengthen robustness against intensity variations, they often inadequately represent the gradual spatial variation of inhomogeneity, ultimately compromising segmentation accuracy. To address this challenge, we introduce a constrained segmentation framework that explicitly

models and compensates for both additive and multiplicative bias fields. The key contributions of our work are summarized as follows:

- A Sobolev-type functional space $W^{1,2}(\Omega)$ is incorporated to regularize the smoothness of both the multiplicative and additive bias fields.
- To more effectively mitigate the interference of multiplicative intensity inhomogeneity on segmentation, we impose a hard constraint on its variation range and incorporate an appropriate edge detection function into the corresponding regularization term.
- The proposed model contains coupled variables and non-smooth terms, which we efficiently address by decomposing the optimization problem into multiple tractable subproblems through alternating direction method (ADM).
- We demonstrate that our proposed model outperforms existing approaches in terms of segmentation accuracy and robustness.

The rest of the paper has the following structure. Section 2 reviews some intensity non-uniformity image segmentation models and related work that are closely related to our proposed model. Section 3 presents the hybrid bias field correction model proposed based on suitable constraints and introduces an efficient numerical algorithm for solving the proposed model. Furthermore, numerical experiments on both natural and medical images are provided in Section 4 to demonstrate the robustness and effectiveness of our model in comparison with several state-of-the-art methods.Conclusions are given in Section 5.

2 Related Works

Assume that $\Omega \in \mathbb{R}^2$ is an open bounded space and the segmented image $I : \Omega \to \mathbb{R}$ is degraded by intensity inhomogeneity or noise interference. In the following, in order to place our work in the context of existing methods, we provide a brief overview of existing segmentation models related to the intensity inhomogeneous image in this section.

2.1 The MS model

The Mumford-Shah model [10] is a foundational variational method in image segmentation problem. It aims to partition an image into homogeneous regions with smooth boundaries while allowing for discontinuities edges where necessary. Specifically, the MS model can be formulated as the following optimization problem:

$$\min_{J,\Gamma} \lambda \int_{\Omega} (J - I)^2 \mathrm{dx} + \mu \int_{\Omega \setminus \Gamma} |\nabla J|^2 \mathrm{dx} + v|\Gamma|, \tag{1}$$

where $|\Gamma|$ was the length of the contour Γ, so that image segmentation can be achieved by minimizing the above function overall contours and fitting the function $J(\mathrm{x})$. However, the solution of the MS model is indeed challenging due to the different nature of the contours Γ and the function $J(\mathrm{x})$, as well as the non-convex nature of the function.

2.2 The L1PS model

By assuming that the observed image is the sum of a segmented constant function c_i for $i = 1, 2$ and a smooth function $b(\mathrm{x})$, Jung in [41] proposed to consider the following optimization problem

$$\begin{aligned} \min_{c_1,c_2,b,u} \int_{\Omega} (I - c_1 - b)^2 u \mathrm{dx} + \int_{\Omega} (I - c_2 - b)^2 (1 - u) \mathrm{dx} + \mu \int_{\Omega} |\nabla b|^2 \mathrm{dx} \\ + \zeta \int_{\Omega} |\nabla u| \mathrm{dx}, \end{aligned} \tag{2}$$

where μ and ζ were the tuning parameter and $|\nabla u(\mathrm{x})| = \sqrt{u_{x_1}^2(\mathrm{x}) + u_{x_2}^2(\mathrm{x})}$ in the total variation (TV) term. The L1PS model dealed well with intensity inhomogeneities and noise. However, the numerical method used to solve the model is not efficient, and the calculation is more complex.

2.3 The ABC model

In [42], Weng et al. proposed an Additive Bias Correction (ABC) model based on nonuniformity of intensity. The model divided the observed image into three parts: additive bias function b , reflection edge structure function r and Gaussian noise n , i.e., $I = b + r + n$, and constructed the energy function as follows:

$$E^{\mathrm{ABC}}(\varphi, r, \mathbf{b}) = \int_{\Omega} \sum_{j=1}^{2} \left(\int_{\Omega} G_{\sigma,\rho}(\mathrm{y}-\mathrm{x}) |I(\mathrm{x}) - r(\mathrm{y}) - b_j(\mathrm{y})|^2 \mathrm{dy} \right) M_j(\varphi(\mathrm{x})) \mathrm{dx}, \tag{3}$$

where the truncated Gaussian function $G_{\sigma,\rho}(\mathrm{y}-\mathrm{x})$ was defined as follows:

$$G_{\sigma,\rho}(\mathrm{y}-\mathrm{x}) = \begin{cases} \frac{1}{\beta} \exp\left(-\frac{\|\mathrm{y}-\mathrm{x}\|^2}{2\sigma^2}\right), & \text{if } \|\mathrm{y}-\mathrm{x}\|_2 \le \rho \\ 0 & \text{, otherwise} \end{cases} \tag{4}$$

for choosing suitable parameters ρ and β. For the two-phase segmentation, the function $M_i(\phi)$ is defined as $M_1(\phi) = H(\phi)$ and $M_2(\phi) = 1 - H(\phi)$ for the Heaviside function with $H(z) = 1$ if $z \ge 0$ and $H(z) = 0$ if $z < 0$. Compared with the traditional segmentation models, this method is more robust and faster. However, due to the different intensity values of the image objects, this model can only segment regions that are darker or brighter and is not suitable for segmenting objects with obvious multicolors.

2.4 The MICO model

By assuming that the image I has two multiplicative components: the reflectance image and the illumination image, Li et al. in [44] proposed a multiplicative intrinsic component optimization (MICO) model for MRI image segmentation. Especially, the MICO model assumed that for a smooth and slowly transforming bias field B can be represented using a given set of smooth basis functions $G := \{g_1(x), \cdots, g_M(x)\}$ linearly combined, guaranteeing the smoothly varying properties of the bias field. Theoretically, a function can be approximated by a linear combination of several basis functions, provided that the number of basis functions is sufficiently large. After choosing the appropriate weights $\mathbf{w} = \{\omega_1, \cdots, \omega_M\}$, b can be expressed as $B(x) = \mathbf{w}^T G$; $t_i(x) = 1$ when $x \in \Omega_i$. Otherwise, $t_i(x) = 0$ for $i = (1, \cdots, N)$. Using the affiliation function t_i and the constant c_i, the true image J can be approximated as:

$$J(X) = \sum_{i=1}^{N} c_i t_i(\mathrm{x}). \tag{5}$$

Based on the above pre-definitions, the MICO model was presented for the case under the binary affiliation function.

$$\min_{\mathbf{t},\mathbf{c},\mathbf{w}} \int_{\Omega} \left| I(\mathrm{x}) - \mathbf{w}^T G(\mathrm{x}) \sum_{i=1}^{N} c_i t_i(\mathrm{x}) \right|^2 \mathrm{dx}. \tag{6}$$

The MICO model minimized the above energy functional by finding the multiplicative intrinsic components B and the true image J of a given image, and many good results can be obtained experimentally. However, the MICO model assumed that the intensity of the true image was piecewise constant, which limited its application in image segmentation and correction, especially when parts of the image have severe bias fields, the MICO model did not work well.

2.5 The LBF model

To better segment the gray scale inhomogeneous images, Li et al. in [35] proposed a Local Binary Fitting (LBF) model by using the local a priori image information, extracting the local features of the image by the Gaussian convolution kernel function $G_\sigma(\mathrm{x}-\mathrm{y})$, and defining an optimization problem as follows:

$$\begin{aligned}\min_{\phi(\mathrm{x}),f_1(\mathrm{x}),f_2(\mathrm{x})} & \lambda_1\int_\Omega\left(\int_\Omega G_\sigma(\mathrm{x}-\mathrm{y})|I(\mathrm{y})-f_1(\mathrm{x})|^2H(\phi(\mathrm{y}))\mathrm{dy}\right)\mathrm{dx}\\ &+\lambda_2\int_\Omega\left(\int_\Omega G_\sigma(\mathrm{x}-\mathrm{y})|I(\mathrm{y})-f_2(\mathrm{x})|^2(1-H(\phi(\mathrm{y})))\mathrm{dy}\right)\mathrm{dx}\\ &+\mu\int_\Omega\frac{1}{2}(|\nabla\phi(\mathrm{x})|-1)^2\mathrm{dx}+\nu\int_\Omega\delta(\phi(\mathrm{x}))|\nabla\phi(\mathrm{x})|\mathrm{dx},\end{aligned} \tag{7}$$

where λ_1 and λ_2 were positive constants, μ and ν are non-negative constants, $f_1(\mathrm{x})$ and $f_2(\mathrm{x})$ was the local fitting function. The third term was used to measure the length of the zero-level set, and the fourth term was used to preserve the stability of the level set as it evolves. The LBF model performs well in inhomogeneous grayscale image, but its numerical method was extremely sensitive to the initial contours and prone to local minima.

2.6 The LIF model

In [36], Zhang et al. proposed a region-based active contour that embeds local information in images by introducing Local Image Fitting (LIF) energy to extract local image information. Its Local Fitting Image (LFI) was defined as:

$$I^{\mathrm{LFI}}=m_1H_\varepsilon(\phi)+m_2(1-H_\varepsilon(\phi)), \tag{8}$$

where m_1 and m_2 were defined as the localised intensity averages inside and outside the contour, denoted as:

$$\begin{cases}m_1=\mathrm{mean}(I\in(\{\mathrm{x}\in\Omega|\phi(\mathrm{x})<0\}\cap\mathcal{W}_k(\mathrm{x})))\\ m_2=\mathrm{mean}(I\in(\{\mathrm{x}\in\Omega|\phi(\mathrm{x})>0\}\cap\mathcal{W}_k(\mathrm{x})))\end{cases} \tag{9}$$

where $\mathcal{W}_k(\mathrm{x})$ denoted the truncated Gaussian window with standard deviation σ of size $(4k+1)\times(4k+1)$ and k was the largest integer less than σ. Following this, it was only necessary to minimize the difference between the fits:

$$\min_{\phi(\mathrm{x})}\lambda\int_\Omega|I-I^{\mathrm{LFI}}|^2\mathrm{dx}. \tag{10}$$

This model was able to segment the image with intensity inhomogeneity and has higher computational efficiency compared to the LBF energy model, but the main drawbacks were the slow segmentation speed and narrow application areas.

2.7 The FISM model

In [50], a two-stage image segmentation method that combines structure tensor and fractional-order regularization was proposed. This model introduced a fractional-order derivative operator under the traditional variational framework as

$$\min_u\frac{\lambda}{2}\int_\Omega|I-u|^2\mathrm{dx}+\frac{\eta}{2}\int_\Omega|\nabla u|^2\mathrm{dx}+\int_\Omega c(\mathrm{x})|\nabla^\alpha u|^2\mathrm{dx}, \tag{11}$$

to enhance the ability to capture image details and boundaries and then used the thresholding method to obtain the segmentation image. Here λ and η were the positive parameter, $\nabla^\alpha u$ denoted the fractional-order gradient operator, $c(x)=k+e^{|\mu_1\mu_2|+|\mu_1-\mu_2|^2}$ for $k>0$, where μ_1 and μ_2 were the eigenvalues of the structure tensor.

Compared with traditional models (such as the CV model), this model performed better in terms of noise robustness, edge preservation, and segmentation accuracy, especially showing remarkable effects in weak boundary and low contrast regions.

2.8 The ACC model

Zhang et al. [51] proposed a new adaptive active contours (AAC) model. By integrating the squared Hellinger distance and multiple truncation functions defined by local correlation features into the level - set framework, it effectively addressed the intensity inhomogeneity and dark edge problems.

$$\begin{aligned} E(\phi) = &\sum_{i=1}^{2} \|[w_l\beta(\frac{1}{2}(I+f_i) - \sqrt{If_i}) + w_g\alpha(\frac{1}{2}(I+c_i) - \sqrt{Ic_i})]M_i(\phi)\| \\ &+ \mu\langle I_s\delta(\phi)|\nabla\phi|, 1\rangle + \nu\langle p(|\nabla\phi|), 1\rangle, \end{aligned} \tag{12}$$

where the parameters μ, ν were positive constant, $M_1(\phi) = H(\phi), M_2(\phi) = 1 - H(\phi)$ and $H(\phi)$ was the Heaviside function. $I_s = |I_m - I_G|$, I_m represented the average intensity of the input image, I_G was the image blurred by a Gaussian filter, defined as $G \otimes I$. $p(\cdot)$ is an energy-density function, defined as

$$p(s) = \frac{1}{2}(s-1)^2. \tag{13}$$

The first term of this model was a global fitting based on the squared Hellinger distance, used to improve the robustness of the initial region and the accuracy of dark blurred regions. The second term was an improved length term. This new length term can slow down or even stop the evolution when the curve approached the target object, while accelerating the overall evolution process of the model. The third term was a penalty term, used to avoid complex and time - consuming reinitialization operations during the curve evolution process. However,this model exhibited high computational complexity, leading to long execution times and relatively low overall efficiency in experiments.

3 The proposed model

To effectively segment image with intensity inhomogeneity interference, it is assumed here that the image can be decomposed into the following model

$$I = b_1 J(\mathrm{x}) + b_2 + n,$$

where b_1 and b_2 denote the multiplicative and additive intensity inhomogeneity respectively, n denotes the noise. Furthermore, we also assume b_1 and b_2 to be smooth and then they are in the space $W^{1,2}(\Omega)$. In addition, $J(\mathrm{x})$ is assumed as the piecewise constant as

$$J(x) = \begin{cases} c_1, \text{ if } \mathrm{x} \in \Omega_1, \\ c_2, \text{ if } \mathrm{x} \in \Omega_2, \end{cases}$$

where Ω_1 is the ROI (region of interest) or called the foreground and $\Omega_2 = \Omega/\Omega_1$ denotes the background of segmentation region.

Based on the above assumptions, we propose the following constrained TV-based segmentation (CTVS) model

$$\begin{aligned} \min_{\substack{u(\mathrm{x})\in\{0,1\} \\ b_1(\mathrm{x})\in\mathcal{E}, b_2(\mathrm{x}) \\ c_1, c_2}} &\overline{\mathcal{G}}(u(\mathrm{x}), b_1(\mathrm{x}), b_2(\mathrm{x}), c_1, c_2) := \lambda \int_\Omega (I(\mathrm{x}) - b_1(\mathrm{x})c_1 - b_2(\mathrm{x}))^2 u(\mathrm{x})\mathrm{dx} \\ &+ \int_\Omega \lambda(I(\mathrm{x}) - b_1(\mathrm{x})c_2 - b_2(\mathrm{x}))^2(1-u(\mathrm{x})) + \alpha g(I(\mathrm{x}))|\nabla b_1(\mathrm{x})|^2 + \beta|\nabla b_2(\mathrm{x})|^2 + |\nabla u(\mathrm{x})|\mathrm{dx}, \end{aligned} \tag{14}$$

where $g(I(\mathrm{x})) = \frac{1}{1+|\nabla I(\mathrm{x})|^2}$ is the edge detection function, λ, α and β are positive weight parameters, and $\mathcal{E} = \{b_1(\mathrm{x}) | \int_\Omega (b_1(\mathrm{x}) - 1)^2 \mathrm{dx} \le \varepsilon\}$[1].

[1] For convenience, unless otherwise specified, the variable x is omitted in the subsequent functionals.

Since(14) is a binary non-convex optimization problem with respect to u and thus difficult to solve numerically, this paper relaxes $\mathcal{C}_2 = \{u \in \mathbb{R}^{m\times n} | u \in \{0,1\}\}$ to its closure $\mathcal{C}_1 = \{u \in \mathbb{R}^{m\times n} | u \in [0,1]\}$ and derives the following relaxed minimization problem.

$$\min_{\substack{u(\mathrm{x})\in[0,1]\\ b_1(\mathrm{x})\in\mathcal{E},b_2(\mathrm{x})\\ c_1,c_2}} \overline{\mathcal{G}}(u(\mathrm{x}), b_1(\mathrm{x}), b_2(\mathrm{x}), c_1, c_2) := \lambda \int_\Omega (I(\mathrm{x}) - b_1(\mathrm{x})c_1 - b_2(\mathrm{x}))^2 u(\mathrm{x})\mathrm{dx}$$
$$+ \int_\Omega \lambda(I(\mathrm{x}) - b_1(\mathrm{x})c_2 - b_2(\mathrm{x}))^2(1-u(\mathrm{x})) + \alpha g(I(\mathrm{x}))|\nabla b_1(\mathrm{x})|^2 + \beta|\nabla b_2(\mathrm{x})|^2 + |\nabla u(\mathrm{x})|\mathrm{dx}. \tag{15}$$

Moreover, as the problem (15) contains the non-smooth term $\int_\Omega |\nabla u(\mathrm{x})|\mathrm{dx}$, which poses significant challenges to numerical solution, it can be approximated by

$$\sqrt{\frac{\pi}{\tau}} \int_\Omega \langle u, G_\tau * (1-u)\rangle \mathrm{dx},$$

where $*$ represents convolution, and

$$G_\tau(x) = \frac{1}{4\pi\tau} \exp(-\frac{|x|^2}{4\tau}).$$

then (15) can be reformulated as the following problem :

$$\min_{\substack{u(\mathrm{x})\in[0,1]\\ b_1(\mathrm{x})\in\mathcal{E},b_2(\mathrm{x})\\ c_1,c_2}} \mathcal{G}(u(\mathrm{x}), b_1(\mathrm{x}), b_2(\mathrm{x}), c_1, c_2) := \lambda \int_\Omega (I(\mathrm{x}) - b_1(\mathrm{x})c_1 - b_2(\mathrm{x}))^2 u(\mathrm{x})\mathrm{dx}$$
$$+ \int_\Omega \lambda(I(\mathrm{x}) - b_1(\mathrm{x})c_2 - b_2(\mathrm{x}))^2(1-u(\mathrm{x})) + \alpha g(I(\mathrm{x}))|\nabla b_1(\mathrm{x})|^2 + \beta|\nabla b_2(\mathrm{x})|^2 + \sqrt{\frac{\pi}{\tau}}\langle u, G_\tau * (1-u)\rangle \mathrm{dx}. \tag{16}$$

To the problem (14) and the problem (16), we can obtain the following relationship.

Theorem 1 *The primal problem* (14) *and the relaxation problem* (16) *are equivalent. In other words, if u^* is a solution to the problem* (14)*, then it is also a solution to the problem* (16)*, and vice versa.*

Proof : First, let

$$\hat{u} = \operatorname*{argmin}_{u\in\{0,1\}} \overline{\mathcal{G}}(u, b_1, b_2, c_1, c_2),$$

it is clear that

$$\overline{\mathcal{G}}(\hat{u}, b_1, b_2, c_1, c_2) \geq \min_{u\in[0,1]} \mathcal{G}(u, b_1, b_2, c_1, c_2). \tag{17}$$

Second, let

$$\tilde{u} = \operatorname*{argmin}_{u\in[0,1]} \mathcal{G}(u, b_1, b_2, c_1, c_2).$$

We now prove by contradiction

$$\tilde{u} = \operatorname*{argmin}_{u\in[0,1]} \mathcal{G}(u, b_1, b_2, c_1, c_2) \in \{0,1\}. \tag{18}$$

Assume the problem (18) does not hold. Then there exists a constant $a > 0$ and a set $A \subset \Omega$ of non-zero measure, such that the minimal solution u^* satisfies

$$u^*(\mathrm{x}) \in (a, 1-a),\ \forall \mathrm{x} \in A.$$

Define the perturbation $u^t = u^* + t\chi_A$ where χ_A is the characteristic function of A. For any $|t| < a$, we have $u^t \in [0,1]$. We compute the first and second derivatives of $\mathcal{G}(u^t, b_1, b_2, c_1, c_2)$ with respect to t . Since

$$\begin{aligned}\mathcal{G}(u^t, b_1, b_2, c_1, c_2) &:= \lambda \int_\Omega (I - b_1c_1 - b_2)^2(u^* + t\chi_A)\mathrm{dx} \\ &+ \int_\Omega \lambda(I - b_1c_2 - b_2)^2(1 - u^* - t\chi_A) + \alpha g(I)|\nabla b_1|^2 + \beta|\nabla b_2|^2 \\ &+ \sqrt{\frac{\pi}{\tau}} \left\langle u^* + t\chi_A, G_\tau * (1 - u^* - t\chi_A)\right\rangle \mathrm{dx}.\end{aligned} \tag{19}$$

we obtain

$$\begin{aligned}\frac{\mathrm{d}\mathcal{G}(u^t, b_1, b_2, c_1, c_2)}{\mathrm{d}t} =& \lambda \left\langle \mathcal{S}, \chi_A\right\rangle + \sqrt{\frac{\pi}{\tau}} \left\langle \chi_A, G_\tau * (1 - u^* - t\chi_A)\right\rangle \\ &+ \sqrt{\frac{\pi}{\tau}} \left\langle u^* + t\chi_A, G_\tau * (-\chi_A)\right\rangle,\end{aligned}$$

where $\mathcal{S} = (I - b_1c_1 - b_2)^2 - (I - b_1c_2 - b_2)^2$. Consequently,

$$\frac{\mathrm{d}^2\mathcal{G}(u^t, b_1, b_2, c_1, c_2)}{\mathrm{d}t^2} = -2\sqrt{\frac{\pi}{\tau}} \left\langle \chi_A, G_\tau * (\chi_A)\right\rangle.$$

Thus

$$\frac{\mathrm{d}^2\mathcal{G}(u^t, b_1, b_2, c_1, c_2)}{\mathrm{d}t^2} < 0,$$

But this contradicts the necessary condition for a minimum that

$$\frac{\mathrm{d}^2\mathcal{G}(u^t, b_1, b_2, c_1, c_2)}{\mathrm{d}t^2} \geq 0.$$

Hence $\tilde{u} \in \{0, 1\}$, and it follows that

$$\mathcal{G}(\tilde{u}, b_1, b_2, c_1, c_2) = \min_{u\in[0,1]} \mathcal{G}(u, b_1, b_2, c_1, c_2) \geq \overline{\mathcal{G}}(\hat{u}, b_1, b_2, c_1, c_2). \tag{20}$$

In summary, we have shown

$$\mathcal{G}(\tilde{u}, b_1, b_2, c_1, c_2) = \min_{u\in[0,1]} \mathcal{G}(u, b_1, b_2, c_1, c_2) = \min_{u\in\{0,1\}} \overline{\mathcal{G}}(u, b_1, b_2, c_1, c_2) = \overline{\mathcal{G}}(\hat{u}, b_1, b_2, c_1, c_2).$$

This completes the proof.

Prior to solving (16), we employ Theorem 2 to demonstrate the existence of a minimizer for model (16).

Theorem 2 *There exists* $(u, b_1, b_2, c_1, c_2) \in BV(\Omega) \times (W^{1,2}(\Omega))^2 \times [0,1]^2$ *to be minimizer of the model* (14)*.*

Proof : The poof easily follows from the direct method in the calculus of variations. We give a sktech of it by the sake of completeness. Since $\overline{\mathcal{G}} \geq 0$ on $L^2(\Omega) \times [0,1]^2$, there exists $m = \inf\left\{\overline{\mathcal{G}}(w, a, b) : (w, a, b) \in L^2(\Omega) \times (W^{1,2}(\Omega))^2 \times [0,1]^2\right\}$. Then, by the compactness property of the TV in $BV(\Omega)$ and the lower semicontinuity of the TV, there exists a minimizer $(u^*(\mathrm{x}), b_1^*, b_2^*, c_1^*, c_2^*) \in BV(\Omega) \times (W^{1,2}(\Omega))^2 \times [0,1]^2$ of $\mathcal{G}$. Since $u_n(\Omega) \subseteq [0,1]$, there is a subsequent (not relabeled) and $u \in L^2(\Omega)$ such that $u_n(x) \to u^*(x)$ weakly in $L^2(\Omega)$ and $u(x) \in [0,1]$ a.e. in Ω. Moreover, from the lower semicontinuity of the anisotropic total variation and coercivity of the $|\cdot|_1$ norm, we may assume that u in $BV(\Omega)$ and that $u_n(x) \to u^*(x)$ in $L^1(\Omega)$.

For the variable b_1: The sequence $b_{1,n}$ belongs to the constraint set $\mathcal{E}$, which implies $\|b_{1,n} - 1\|_{L^2}^2 \leq \varepsilon$, so $\{b_{1,n}\}$ is bounded in $L^2(\Omega)$. The regularization term $\alpha \int g(I)|\nabla b_{1,n}|^2\mathrm{dx}$ is bounded. Since the edge function $g(I) = \frac{1}{1+|\nabla I|^2}$ is strictly positive and bounded, the gradient $\|\nabla b_{1,n}\|_{L^2}$ is uniformly bounded. Therefore, $\{b_{1,n}\}$ is bounded in the Sobolev space $W^{1,2}(\Omega)$. By the Rellich-Kondrachov Compactness Theorem, the embedding

$W^{1,2}(\Omega) \to L^2(\Omega)$ is compact. Thus, there exists a subsequence such that: $b_{1,n} \to b_1^*$ weakly in $W^{1,2}(\Omega)$ and $b_{1,n} \to b_1^*$ strongly in $L^2(\Omega)$.

For the variable b_2: Similarly, the coercivity of the fidelity term ensures $b_{2,n}$ is bounded in L^2, and the term $\beta \int |\nabla b_{2,n}|^2 \mathrm{dx}$ ensures boundedness in $W^{1,2}(\Omega)$ semi-norm. Thus, $b_{2,n} \to b_2^*$ weakly in $H^1(\Omega)$ and strongly in $L^2(\Omega)$. On the other hand, since $c_{i,n} \in [0,1]$ for $i = 1, 2$, then there is a subsequence (not relabeled) and $c_i^* \in [0,1]$ such that $c_{i,n} \to c_i^*$ for $i = 1, 2$.

Finally, using the lower semicontinuity of the TV term and the convergence of the fidelity terms, we obtain

$$\overline{\mathcal{G}}(u^*(\mathrm{x}), b_1^*, b_2^*, c_1^*, c_2^*) \leq \liminf_{n\to\infty} \overline{\mathcal{G}}(u_n(\mathrm{x}), b_{1,n}, b_{2,n}, c_{1,n}, c_{2,n}) = m,$$

which shows that $(u^*(\mathrm{x}), b_1^*, b_2^*, c_1^*, c_2^*)$ is a minimizer.

The proposed CTVS model (14) involves solving a multivariable, non-convex and non-smooth optimization problem. To address this efficiently, it is critical to decouple the interdependent variables or operators. Toward this objective, we employ the alternating direction method (ADM) to reformulate it into the following optimization framework[2]:

$$\begin{cases} u^{\ell+1} = \underset{u\in[0,1]}{\operatorname{argmin}} \mathcal{G}\left(u, b_1^\ell, b_2^\ell, c_1^\ell, c_2^\ell\right), & (21) \\ b_1^{\ell+1} = \underset{b_1\in\mathcal{E}}{\operatorname{argmin}} \mathcal{G}\left(u^{\ell+1}, b_1, b_2^\ell, c_1^\ell, c_2^\ell\right), & (22) \\ b_2^{\ell+1} = \underset{b_2}{\operatorname{argmin}} \mathcal{G}\left(u^{\ell+1}, b_1^{\ell+1}, b_2, c_1^\ell, c_2^\ell\right), & (23) \\ c_1^{\ell+1} = \underset{c_1}{\operatorname{argmin}} \mathcal{G}\left(u^{\ell+1}, b_1^{\ell+1}, b_2^{\ell+1}, c_1, c_2^\ell\right), & (24) \\ c_2^{\ell+1} = \underset{c_2}{\operatorname{argmin}} \mathcal{G}\left(u^{\ell+1}, b_1^{\ell+1}, b_2^{\ell+1}, c_1^{\ell+1}, c_2\right). & (25) \end{cases}$$

Therefore, we can clearly draw the following conclusions: the objective function is monotonically non-increasing at each iteration.

$$\mathcal{G}(u^{\ell+1}, b_1^{\ell+1}, b_2^{\ell+1}, c_1^{\ell+1}, c_2^{\ell+1}) \leq \mathcal{G}(u^\ell, b_1^\ell, b_2^\ell, c_1^\ell, c_2^\ell).$$

This ensures the stability of the algorithm during iterations and guarantees convergence to a stationary point.

In the following, we consider how to solve the subproblems (21)-(25).

– **Solving subproblem** (21). Specifically, the proposed ICTM method is considered to solve the problem (21), we linearize it at $u^{\ell,k}$ then the subproblem (21) can be approximately rewritten as

$$u^{\ell,k+1} = \underset{u\in[0,1]}{\operatorname{argmin}} \langle \phi\left(u^{\ell,k}\right), u\rangle, \tag{26}$$

where $\phi\left(u^{\ell,k}\right) = \lambda S^\ell - \sqrt{\frac{\pi}{\tau}} G_\tau * \left(1 - 2u^{\ell,k}\right)$. This is a concave optimization problem, and the optimal solution is attained at the endpoints. That is to say, the minimizer $u^{\ell,k+1}$ satisfies that

$$u^{\ell,k+1} = \begin{cases} 1, & \text{if } \phi\left(u^{\ell,k}\right) \leq 0 \\ 0, & \text{otherwise} \end{cases} \tag{27}$$

– **Solving subproblems** (22) **and** (23). These subproblems are convex and smooth and the optimization conditions satisfy that

$$\begin{cases} \left(\lambda\left(c_1^\ell\right)^2 u^{\ell+1}\mathcal{I} + \lambda\left(c_2^\ell\right)^2\left(1-u^{\ell+1}\right)\mathcal{I} - \alpha g(I)\Delta\right) b_1^{\ell+1} = \lambda\left(I - b_2^\ell\right)\left(c_1^\ell u^{\ell+1} + c_2^\ell(1-u^{\ell+1})\right) & (28) \\ \left(\lambda\mathcal{I} - \beta\Delta\right) b_2^{\ell+1} = \lambda\left(I - b_1^{\ell+1}(c_1^\ell u^{\ell+1} + c_2^\ell\left(1-u^{\ell+1}\right))\right) & (29) \end{cases}$$

[2] In the following discussions, for brevity and without loss of clarity , we omit the variable x in the functions.

with the suitable boundary condition, where $\mathcal{I}$ is the identity matrix. Here we assume that discretization of the equations (28) and (29) is of using the periodic boundary condition, then the solutions can be obtained by using the FFT as

$$\begin{cases} b_1^{\ell+1} = \mathcal{F}^{-1}\left(\dfrac{\mathcal{F}[\lambda(I-b_2^\ell)(c_1^\ell u^{\ell+1}+c_2^\ell(1-u^{\ell+1}))]}{\mathcal{F}[\lambda(c_1^\ell)^2u^{\ell+1}+\lambda(c_2^\ell)^2(1-u^{\ell+1})-\alpha g(I)\Delta]}\right), & (30) \\ b_2^{\ell+1} = \mathcal{F}^{-1}\left(\dfrac{\mathcal{F}[\lambda(I-b_1^{\ell+1}(c_1^\ell u^{\ell+1}+c_2^\ell(1-u^{\ell+1}))]}{\mathcal{F}[\lambda-\beta\Delta]}\right). & (31) \end{cases}$$

– **Solving subproblems** (24) **and** (25). These problems are equivalent to:

$$\begin{cases} c_1^{\ell+1} := \underset{c_1}{\operatorname{argmin}} \displaystyle\int_\Omega \left(I-b_1^{\ell+1}c_1-b_2^{\ell+1}\right)^2 u^{\ell+1}\mathrm{dx} & (32) \\ c_2^{\ell+1} := \underset{c_2}{\operatorname{argmin}} \displaystyle\int_\Omega \left(I-b_1^{\ell+1}c_2-b_2^{\ell+1}\right)^2 \left(1-u^{\ell+1}\right)\mathrm{dx} & (33) \end{cases}$$

They are the convex and smooth optimization problem and the closed-form solutions can be obtained by

$$\begin{cases} c_1^{\ell+1} = \dfrac{\int_\Omega \left(I-b_2^{\ell+1}\right) b_1^{\ell+1}u^{\ell+1}\mathrm{dx}}{\int_\Omega (b_1^{\ell+1})^2 u^{\ell+1}\mathrm{dx}} & (34) \\ c_2^{\ell+1} = \dfrac{\int_\Omega \left(I-b_2^{\ell+1}\right) b_1^{\ell+1}\left(1-u^{\ell+1}\right)\mathrm{dx}}{\int_\Omega (b_1^{\ell+1})^2 \left(1-u^{\ell+1}\right)\mathrm{dx}} & (35) \end{cases}$$

More specifically, the algorithm to solve the model(14) is summarized as follows.

Algorithm 1 The algorithm of the hybrid bias field correction image segmentation model (14).

Input: Input image I, parameters λ, α, $\beta > 0$. maximum outer iteration L_{max} .
maximum inner iteration K_{max} and stopping threshold ϵ.
Initialize: Set $b_1^0 = \mathbf{1}$, $b_2^0 = \mathbf{0}$, $u^0 = \mathbf{0}$, c_i^0.
Iterative Solution $u^{\ell+1}, b_1^{\ell+1}, b_2^{\ell+1}, c_1^{\ell+1}, c_2^{\ell+1}$
while $\ell \le L_{max}$ **do**
  while $k \le K_{max}$ or $\frac{\|u^{\ell,k+1}-u^{\ell,k}\|_1}{\|u^{\ell,k}\|_1} > \epsilon$ **do**
    Update $u^{\ell,k+1}$ according to (27)
    $k := k+1$
  then
  set $u^{\ell+1} := u^{\ell,k+1}$
  Update $b_1^{\ell+1}$ according to (30)
  Update $b_2^{\ell+1}$ according to (31)
  Update $c_1^{\ell+1}$ according to (34)
  Update $c_2^{\ell+1}$ according to (35)
  $\ell := \ell+1$
end
Output: Segmentation result $u := u^{\ell+1}$

4 Numerical Results

In this section, we present the numerical experiments of the proposed model in various image labeling and segmentation applications. To prove the effectiveness and superiority of our proposed CTVS model, we compared it with seven advanced methods, such as ICTM [17], ICTMB [19], L1PS [41], LBF [35], LIF [36], WBHMS [52] and ABC [42], in synthetic and real images. To make the experimental comparison as fair as possible, the parameters of the comparative methods are selected as suggested in the corresponding papers. All numerical experiments are performed in a Matlab R2020b environment on a desktop with 3.20GHz Intel(R) Core(TM) i5-6500 CPU and 8GB RAM.

4.1 Parameter rules

Here we discuss the choices of the parameters used in our proposed model and the models of the comparative experiment. Throughout all experiments, we set the maximum number of iterations as $L_{max} = 300$ and the termination condition error is $\epsilon = 10^{-4}$. The variables involved in our method are the fidelity parameter of the data λ, the weights α and β of the bias field, the number of inner cycles K_{max} for u. Parameters were tuned empirically to achieve optimal segmentation performance across the test datasets. In the natural image, we set $\lambda \in [10, 30]$, $\alpha = 30$, $\beta \in [30, 60]$, respectively. In the MRI, we set $\lambda \in [4, 7]$, $\alpha = 30$, $\beta \in [48, 52]$, respectively.When updating u, the parameter τ in the heat-kernel convolution is determined by the three-sigma rule for MRI image segmentation, while for natural image segmentation, the range of τ is set to $[0.04, 1.9]$.

Next, we consider the range of parameters involved in the comparative models. We refer to the corresponding literature and then adjust the parameters to obtain ideal results. The related details are summarized as follows.

1) ICTM: The ICTM model is an efficient iterative thresholding method, the parameters are the data fidelity parameter $\lambda \in [0.02, 0.09]$ and the time step $\delta \in [0.26, 0.03]$.
2) ICTMB: The ICTMB model proposes a novel hybrid bias field correction model by decoupling the multiplicative bias field and the additive bias field, the parameters are the data fidelity parameter $\lambda \in [1.8, 11]$ and the weights $\alpha = 30$ and $\beta \in [30, 60]$.
3) L1PS: For the L1PS model, the parameter of the data fidelity term $\lambda \in [1, 10^3]$, the parameter of the length term $\nu \in [0, 900]$, the smooth term parameter $\alpha \in [1 \times 10^4, 5 \times 10^4]$, the penalty parameters $r_1 = \{0, 90\}$.
4) LBF: The force term parameters are chosen from $\lambda_1 = 1$ and $\lambda_2 = 1$. The level set regularization term parameter is set as $\mu = 1$, the length term parameter is set as $\nu \in [1.7 \times 10^4, 1 \times 10^5]$. The Gaussian kernel parameter is chosen from $\sigma \in [1, 22]$.
5) LIF: The Gaussian kernel parameter is chosen from $\sigma \in [34, 80]$. The constant for the Heaviside-Dirac function is set as $\epsilon = 1$. The time step is set as $\Delta t = 1$.
6) WBHMS: The WBHMS model is a weighted bounded Hessian variational model. In the natural image, we set the value ranges of the piecewise constants $c_1 \in [1 \times 10^{-4}, 1 \times 10^{-2}]$ and $c_2 \in [0.40, 0.55]$. In the MRI, we set the value ranges of piecewise constants $c_1 \in [0.09, 0.20]$ and $c_2 \in [0.48, 0.57]$.
7) ABC: The ABC model, an additive bias correction (ABC) model based on intensity inhomogeneity, is proposed. we set the weight parameter $\alpha \in [1, 5]$, the scale parameters of the Gaussian function $\sigma \in [5, 100]$.

4.2 Evaluation Indicators

In this part of the numerical experiment, we use four metrics, namely Jaccard similarity, accuracy, F1-Score, κ coefficient, to objectively evaluate the results of the segmentation. The closer the values of these indicators are to 1, the closer the experimental results are to the ground truth. Next, we discuss the influence of different images and parameters in the experiments on the results.

1) Jaccard Similarity (JS) coefficient is used to measure the similarity and difference between the segmentation result S_1 and the ground truth S_2. JS is defined as:

$$\mathrm{JS} = \frac{|S_1 \cap S_2|}{|S_1 \cup S_2|},$$

where $|\cdot|$ represents the number of pixels in the image area.
2) Pixel accuracy is a common evaluation index to evaluate the segmentation result. It is used to calculate the percentage of pixels correctly classified in the segmentation results of the model. $\mathrm{Accuracy}$ is defined as:

$$\mathrm{Accuracy} = \frac{\mathrm{TP} + \mathrm{TN}}{\mathrm{TP} + \mathrm{TN} + \mathrm{FP} + \mathrm{FN}},$$

where TP represents the number of real samples, TN represents the number of true negative samples, FP represents the number of false positive samples, FN represents the number of false negative samples.

3) In the two-phase segmentation problem, the F1 score is a measure of the precision of the segmentation results. This measure integrates the accuracy and recall of model segmentation results and is a harmonic average of these two evaluation indexes. The F1 score (F1) is defined as:

$$\mathrm{F1} = \frac{2\mathrm{PR}}{\mathrm{P}+\mathrm{R}}, \text{ with } \mathrm{P} = \frac{\mathrm{TP}}{\mathrm{TP}+\mathrm{FP}} \text{ and } \mathrm{R} = \frac{\mathrm{TP}}{\mathrm{TP}+\mathrm{FN}}.$$

4) κ-coefficient is an index to measure classification accuracy based on confusion matrix and is defined as

$$\kappa = \frac{\mathrm{ACC}-\mathrm{P_c}}{1-\mathrm{P_c}}, \text{ with } \mathrm{P_c} = \frac{(\mathrm{TP}+\mathrm{FN})(\mathrm{TP}+\mathrm{FP})+(\mathrm{FP}+\mathrm{TN})(\mathrm{FN}+\mathrm{TN})}{(\mathrm{TP}+\mathrm{TN}+\mathrm{FP}+\mathrm{FN})^2}.$$

4.3 Effectiveness analysis of bias field correction

We have experimentally verified the effectiveness of the model in terms of polarization field correction. In this paper, we consider the simultaneous existence of two bias fields under complex natural conditions and remove both bias fields at once in the model. It is also compared with the common additive bias correction model L1PS [41] and the multiplicative bias correction model MICO [44]. Figure 1 gives a 3D image of the grayscale distribution of the original and corrected images. The LIPS model oversmoothes, resulting in reduced image contrast; the MICO model preserves image contrast, but does not get a significant correction for the uneven gray fraction of the image. Figure 1 (d) shows the correction effect of our proposed model, where the distribution of the final pixel values is smooth and regular. The features of the pixel distribution in the target region are well preserved, and the gray scale in the background is relatively uniform. Therefore, the model performs bias field correction to a large extent, ensuring the uniformity of the gray scale of the image to be segmented, which largely improves the accuracy and efficiency of the subsequent segmentation.

4.4 Robustness for initialization

This section employs numerical experiments to verify the robustness of initialization. The first row of Figure2 illustrates four different initial contour settings, from left to right: a square located inside the object, a rectangle intersects the object, a circle located inside the object and fully enclosing the object. The second row displays the correspongding segmentation results produced by the proposed model. The performance of our proposed CTVS model for different initial contours is evaluated by segmenting the natural image with four different initializations. As can be seen in Figure 2, there is no significant difference in the final segmentation results for these different initializations, with the corresponding active contours consistently outlining the target boundaries. It is evident that our proposed CTVS model produces an identical LS function across all four initializations.

To evaluate the robustness of different methods to initial contours, we configure four distinct initial contours in Figure 3. Each method is tested under these configurations, and the corresponding results are summarized in Table 1. The CTVS model achieved the best overall performance across all tested initial contours. Its JS, SA and F1-score were significantly higher than those of the other compared methods in most cases, demonstrating the strongest robustness and stability. For instance, across the four contours, the JS of CTVS was close to or exceeded 0.989, its accuracy was above 0.986, and its F1-score was no less than 0.994, indicating its low sensitivity to the setting of the initial contour.

4.5 Natural Images

Here, we evaluate our proposed CTVS model quantitatively and compare it with the previously mentioned models. The original dataset is downloaded from the website [3]. To simulate a realistic complex scenario, we considere the implantation of bias fields for the selected images, and test images are shown in Figure 4, where we number and the initial contours are chosen for the experiments. Under controlled conditions, the same initial contour is applied consistently to all compared methods for every test image.

[3] https://www.wisdom.weizmann.ac.il/ $\sim$ vision.

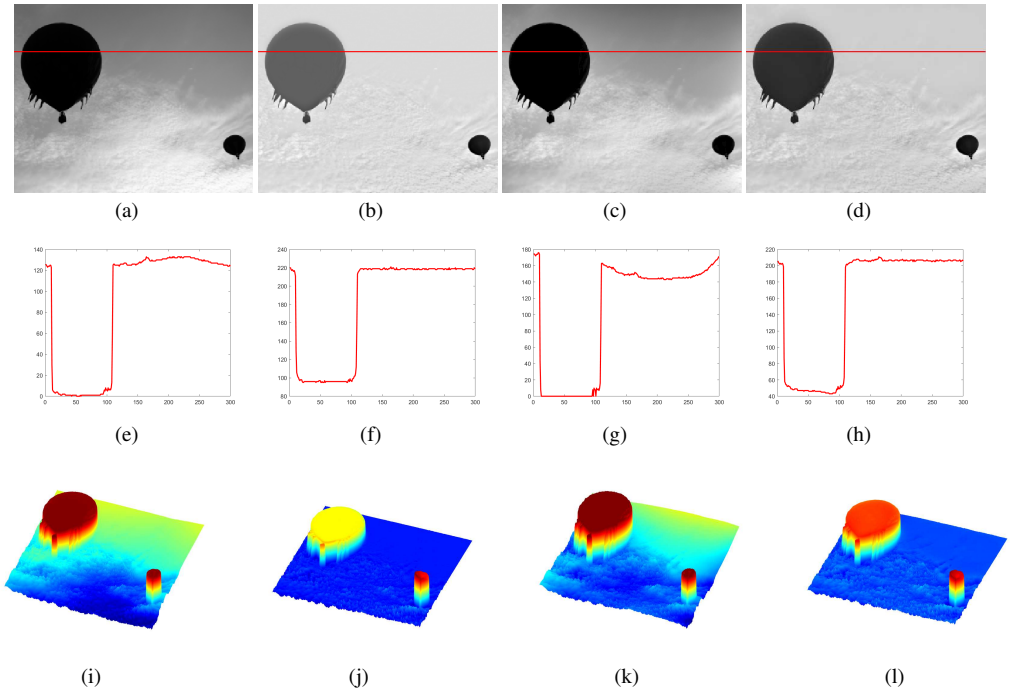


Fig. 1: Effectiveness analysis of bias field correction. The first row shows the original image, the L1PS model-corrected image, the MICO model-corrected image, and the CTVS model-corrected image, respectively; The second row is the 60th row of pixel values of the images displayed in the first row; The third row is the 3D surface plots of the images shown in the first row.

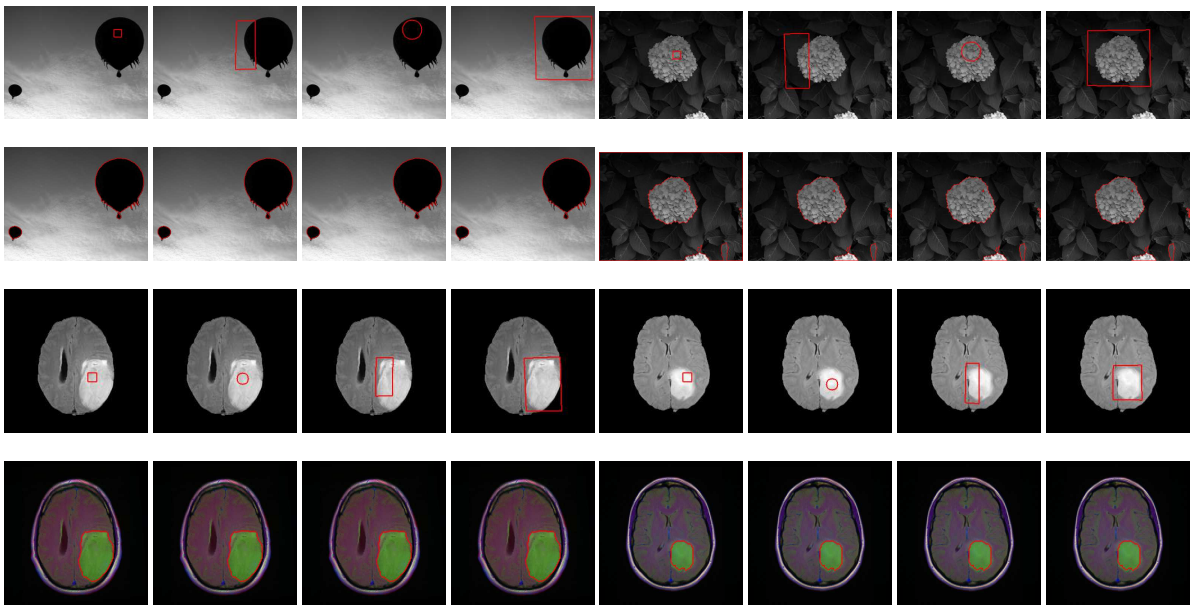


Fig. 2: Segmentation results under different initial contours .

To validate the effectiveness and robustness of the proposed model, segmentation experiments are conducted on the test images shown in Figure 4. The initial contours used in the experiments are presented in Figure 5.

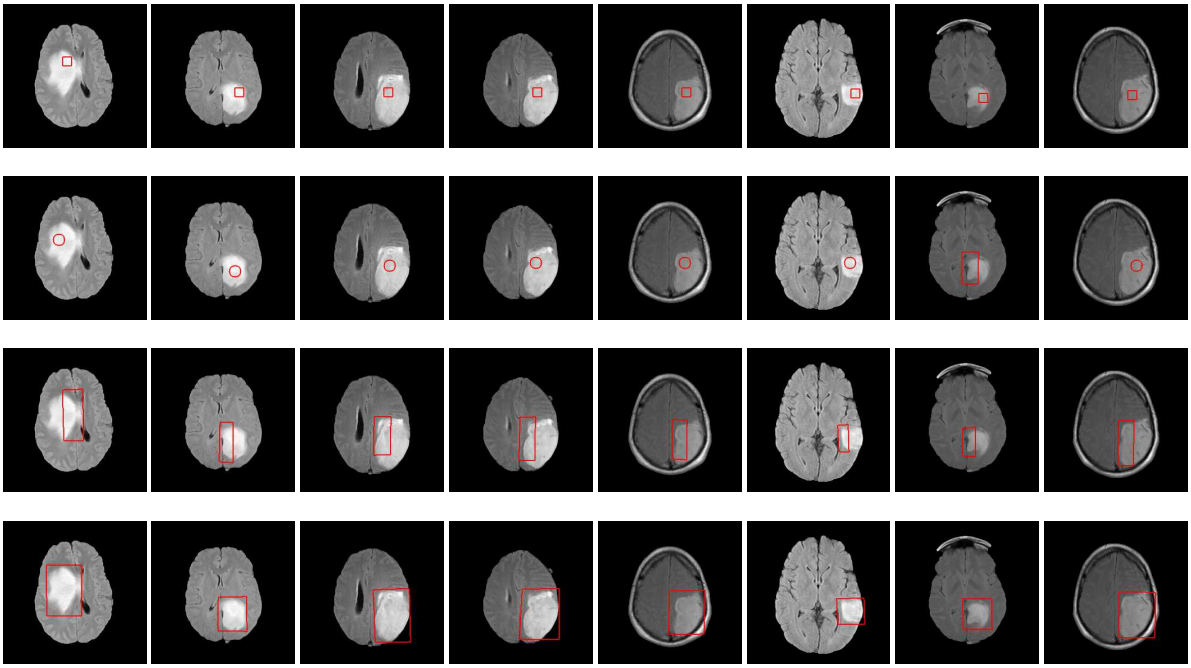


Fig. 3: MRI figures under different initial contours.

Criterions	JS								Accuracy							
contours	ICTM	ICTMB	L1PS	LBF	LIF	WBHMS	ABC	CTVS	ICTM	ICTMB	L1PS	LBF	LIF	WBHMS	ABC	CTVS
contour1	0.7958	0.9905	0.7208	0.5949	0.9917	0.9661	0.7393	**0.9955**	0.9823	0.9912	0.9854	0.9802	0.9921	0.9674	0.9783	**0.9953**
contour2	0.6720	0.6487	0.5793	0.5738	0.9601	0.9726	0.5563	**0.9899**	0.9768	0.9782	0.9798	0.9705	0.9616	0.974	0.9597	**0.9862**
contour3	0.7660	0.5999	0.6654	0.5396	0.9691	0.9764	0.5397	**0.9899**	0.9882	0.9842	0.9737	0.9644	0.9705	0.9775	0.9566	**0.9862**
contour4	0.7660	0.7235	0.7058	0.4494	0.9694	0.9738	0.5596	**0.9899**	0.9793	0.9799	0.9801	0.9311	0.97085	0.9743	0.9593	**0.9862**
Criterions	F1-score								κ							
contours	ICTM	ICTMB	L1PS	LBF	LIF	WBHMS	ABC	CTVS	ICTM	ICTMB	L1PS	LBF	LIF	WBHMS	ABC	CTVS
contour1	0.8824	0.9865	0.8266	0.7417	0.9958	0.9815	0.8387	**0.9978**	0.8765	0.9445	0.8193	0.7317	0.8994	0.6649	0.8285	**0.9492**
contour2	0.7995	0.7869	0.7336	0.7228	0.9792	0.9861	0.6911	**0.9947**	0.7995	0.7836	0.7238	0.7084	0.6806	0.7867	0.6720	**0.9003**
contour3	0.8613	0.7499	0.7991	0.6938	0.9843	0.988	0.69	**0.9947**	0.8613	0.7418	0.785	0.677	0.7083	0.8028	0.6702	**0.9003**
contour4	0.8302	0.8396	0.8275	0.6067	0.9844	0.9867	0.7021	**0.9947**	0.8302	0.836	0.8171	0.5810	0.7312	0.5726	0.6834	**0.9003**

Table 1: The index values of the segmentation results of our model and the comparison models in MRI images with different initial contours .

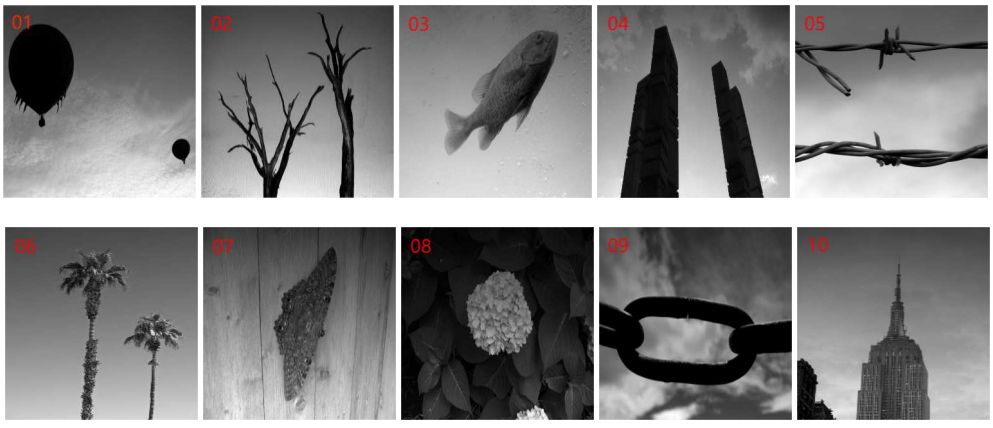


Fig. 4: Natural image after implantation of bias field.

The segmentation results of our proposed CTVS model and comparative models in natural images are shown

in Figure 6. As summarized in Table 2, the proposed CTVS model achieves the highest average scores across all four metrics (JS, Accuracy, F1-score, and κ), indicating its overall superior segmentation accuracy and consistency.The experimental results confirm that the model is capable of effectively processing and accurately segmenting natural images even in the presence of severe bias fields.

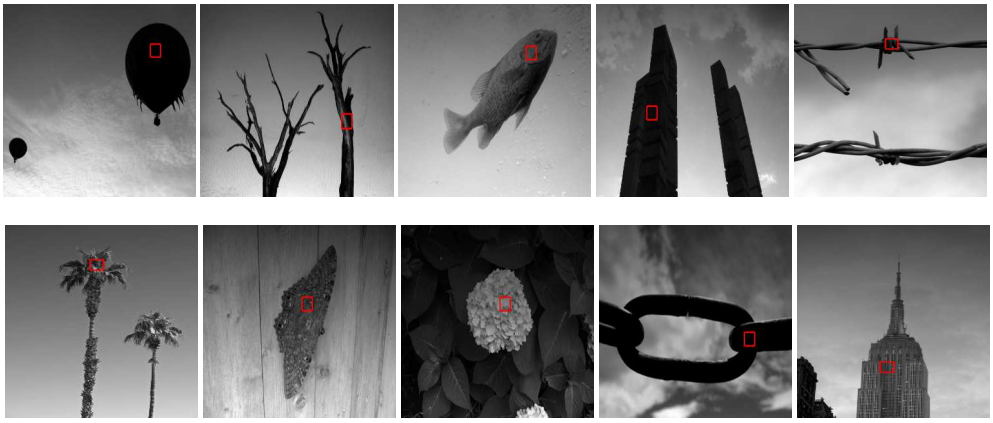


Fig. 5: The initial contours of nature images.

Criterions	JS								Accuracy							
Images	ICTM	ICTMB	L1PS	LBF	LIF	WBHMS	ABC	CTVS	ICTM	ICTMB	L1PS	LBF	LIF	WBHMS	ABC	CTVS
01	0.9813	0.9819	0.9808	0.4204	0.6335	0.9961	0.4371	0.9973	0.9975	0.9976	0.9975	0.8323	0.6364	0.9966	0.8417	0.9976
02	0.7364	0.8436	0.8218	0.8688	0.8902	0.9618	0.8477	0.9754	0.9640	0.9783	0.9754	0.9816	0.9033	0.9658	0.9763	0.9783
03	0.7403	0.8629	0.8353	0.8750	0.8475	0.9304	0.5284	0.9941	0.9546	0.9760	0.9712	0.9780	0.8707	0.9389	0.8661	0.9951
04	0.9432	0.9939	0.9942	0.9227	0.9617	0.9910	0.8315	0.9978	0.9830	0.9983	0.9984	0.9763	0.9725	0.9935	0.9438	0.9984
05	0.7036	0.8295	0.7461	0.8665	0.9555	0.9509	0.7031	0.9704	0.9564	0.9748	0.9984	0.9801	0.9610	0.9560	0.9512	0.9740
06	0.3461	0.8452	0.7191	0.8107	0.9653	0.9118	0.3774	0.9780	0.9495	0.9803	0.9656	0.9758	0.9687	0.9183	0.8382	0.9804
07	0.7909	0.9102	0.8288	0.9090	0.6794	0.8897	0.3664	0.9915	0.9719	0.9872	0.9782	0.9873	0.7212	0.8961	0.7340	0.9926
08	0.9343	0.9594	0.9505	0.9424	0.9882	0.9942	0.4800	0.9954	0.9920	0.9950	0.9951	0.9929	0.9896	0.9949	0.8740	0.9960
09	0.9085	0.8720	0.7461	0.5248	0.7563	0.9711	0.5343	0.9665	0.9772	0.9661	0.9214	0.7899	0.8125	0.9776	0.7865	0.9740
10	0.7031	0.9601	0.9531	0.9559	0.8129	0.8636	0.4643	0.9907	0.9363	0.9922	0.9908	0.9914	0.8486	0.8777	0.7748	0.9924
Mean	0.7788	0.9059	0.8756	0.8096	0.8491	0.9461	0.5570	**0.9857**	0.9652	0.9846	0.9756	0.9486	0.8685	0.8777	0.8587	**0.9879**
Criterions	F1-score								κ							
Images	ICTM	ICTMB	L1PS	LBF	LIF	WBHMS	ABC	CTVS	ICTM	ICTMB	L1PS	LBF	LIF	WBHMS	ABC	CTVS
01	0.9906	0.9909	0.9924	0.5919	0.7756	0.9981	0.6083	0.9986	0.9892	0.9895	0.9890	0.5040	0.8443	0.9851	0.5247	0.9895
02	0.8484	0.9151	0.9025	0.9289	0.9419	0.9805	0.9176	0.9876	0.8284	0.9028	0.8885	0.9193	0.6567	0.8394	0.9038	0.9026
03	0.8508	0.9264	0.9102	0.9333	0.9714	0.9639	0.6914	0.9970	0.8247	0.9122	0.8933	0.9202	0.6227	0.7656	0.6100	0.9828
04	0.9708	0.9969	0.9971	0.9598	0.9805	0.9955	0.9080	0.9989	0.9588	0.9957	0.9960	0.9430	0.9340	0 .9840	0.8678	0.9962
05	0.8262	0.9068	0.8546	0.9258	0.9772	0.9748	0.8257	0.9850	0.8021	0.8924	0.8336	0.9169	0.8412	0.8002	0.7974	0.8885
06	0.5142	0.9161	0.8390	0.8955	0.9823	0.9539	0.5480	0.9889	0.4813	0.9050	0.8203	0.8819	0.8442	0.5953	0.4610	0.9051
07	0.8833	0.9530	0.9210	0.9523	0.8093	0.9416	0.4919	0.9958	0.8675	0.9456	0.9084	0.9450	0.3516	0.4744	0.3664	0.9681
08	0.9660	0.9793	0.9795	0.9703	0.9941	0.9971	0.6487	0.9977	0.9615	0.9764	0.9767	0.9663	0.9515	0.9757	0.5815	0.9808
09	0.9521	0.9316	0.8546	0.6883	0.8613	0.9853	0.6965	0.9830	0.9372	0.9091	0.8012	0.5457	0.5831	0.9384	0.5525	0.9280
10	0.8257	0.9796	0.9760	0.9774	0.8968	0.9268	0.6341	0.9953	0.7869	0.9748	0.9704	0.9721	0.6223	0.5585	0.5010	0.9756
Mean	0.8628	0.9496	0.9225	0.8824	0.9136	0.9718	0.6970	**0.9928**	0.8438	0.9404	0.9077	0.8514	0.7252	0.7917	0.6166	**0.9517**

Table 2: The index values of the segmentation results of our model and the comparison models in natural images.

4.6 Segment glioma for MRI.

Gliomas, the most common primary malignant tumors of the central nervous system, originate from neuroglial cells and account for approximately 30% of all brain tumors and over 80% of malignant brain tumors. According to the World Health Organization (WHO) classification system, gliomas are graded from I to IV. High-grade gliomas, such as glioblastoma multiforme (GBM, WHO grade IV), are characterized by highly invasive growth, rapid proliferation, and poor prognosis, with a median overall survival typically less than 15 months. Pathological features include diffusely infiltrative growth, marked cellular and molecular heterogeneity, and frequent peritumoral edema and necrotic regions. These characteristics result in poorly defined boundaries between

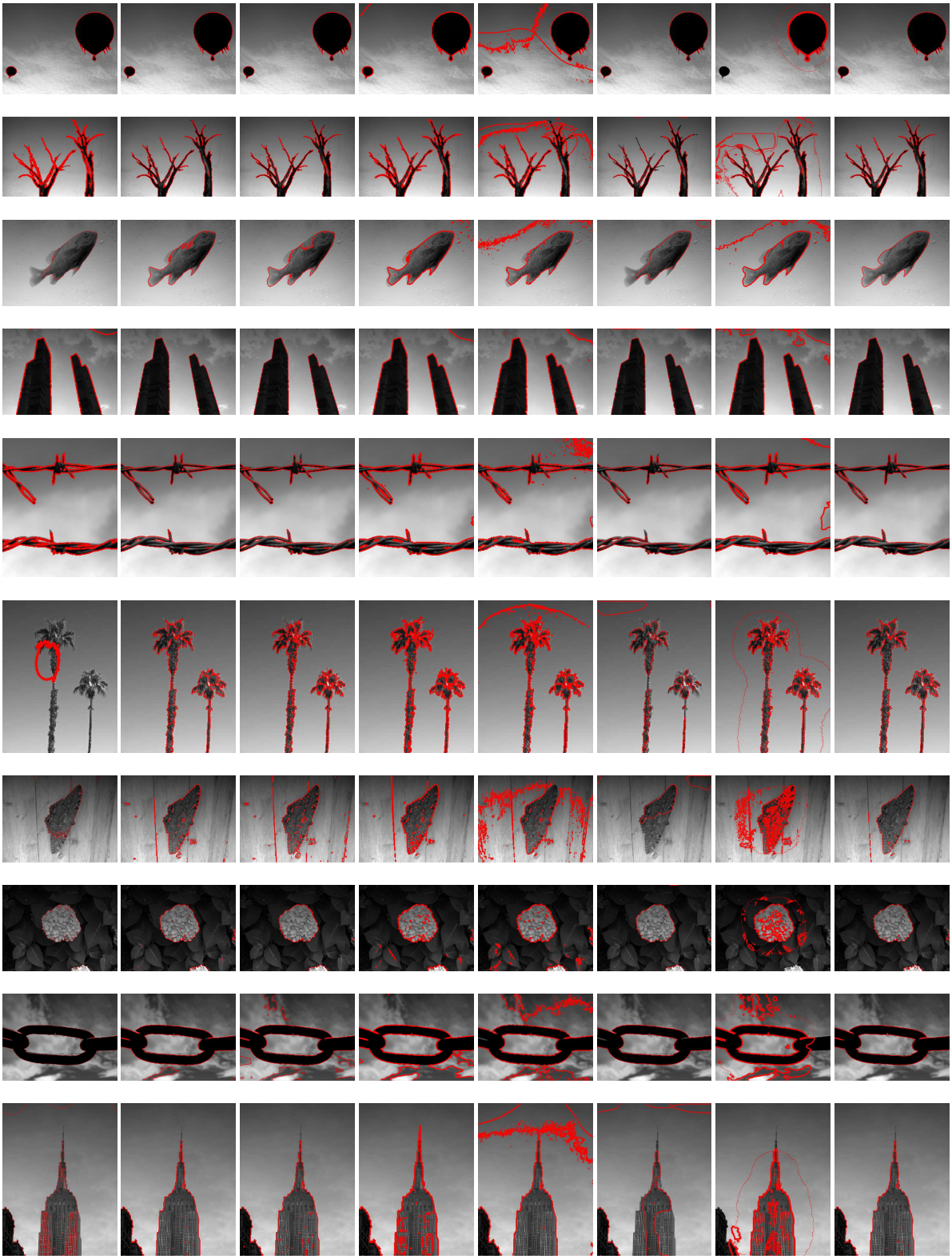


Fig. 6: Segmentation results of comparative models in natural images .

the tumor and normal brain tissue, posing significant challenges for accurate diagnosis and treatment. To compare the differences between the relevant models and the proposed CTVS model to segment the glioma image, we select ten brain MRI images downloaded from the website [4] for our experiments in Figure 7.

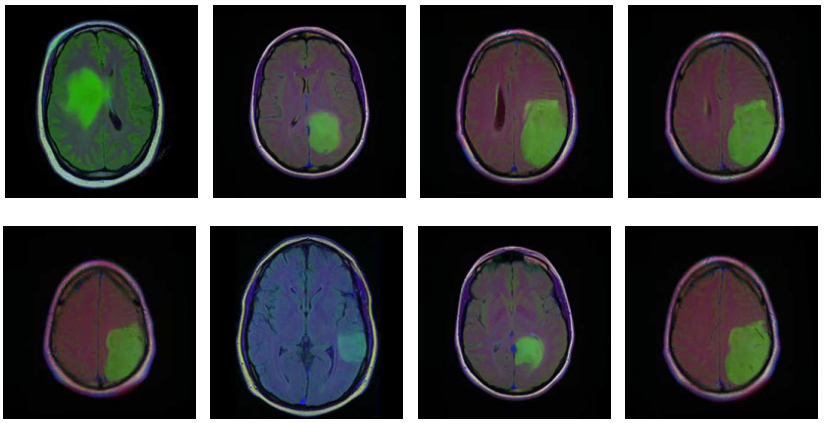


Fig. 7: Magnetic resonance images downloaded from the kaggle dataset.

To minimize errors in subsequent segmentation, skull stripping was first applied to the images in Figure 7. This paper is based on a morphological approach to an automated skull stripping technique through threshold segmentation and morphological erosion and expansion operations. It should be noted that gliomas in MRI have edematous borders and complex internal structures, so segmentation of gliomas and their internal structures can be difficult. In terms of initial contour selection, a new selection method is used in this paper. After graying out the image and using the high brightness feature of the glioma after stripping the skull, the image values of each row and column of the image are summed separately to obtain the row and column with the largest image value. Assuming the coordinates of the intersection of the row and column are $[x, y]$, the initial contour is defined as $[x-15, x+15] \times [y-15, y+15]$. The results of skull stripping and initial contour selection in this paper are shown in Figure 9. The segmentation results of the glioma between our proposed CTVS model and the comparative models in MRI images are shown in Figure 8.

[4] https://www.kaggle.com/datasets/mateuszbuda/lgg-mri-segmentation

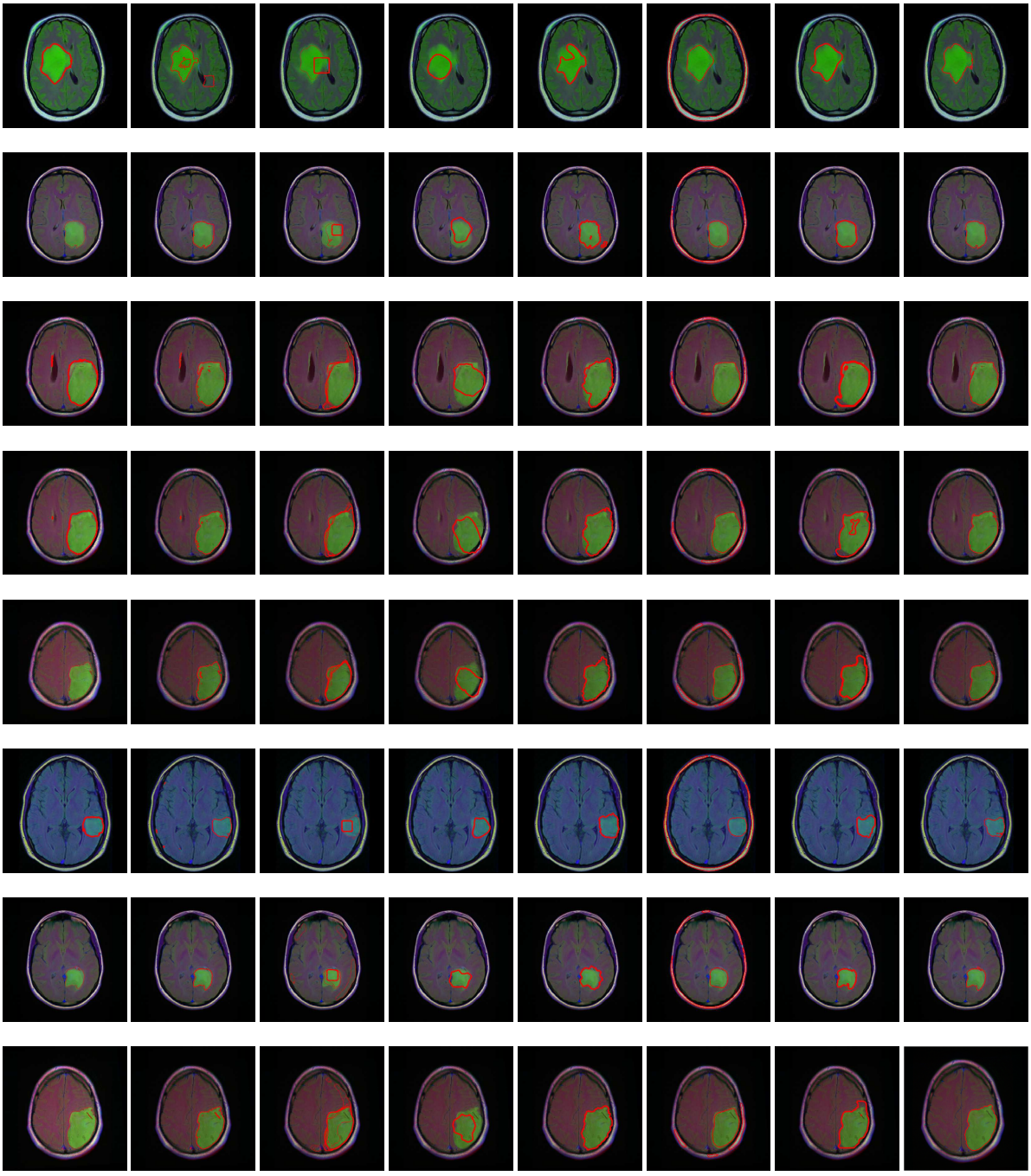


Fig. 8: Segmentation results of comparative models in MRI images .

Note the edematous margins and the complex internal structure of the glioma. Figure 10 shows the original image, the region of the injury and the details of the experimental results of ICTM [17], ICTMB [19], L1PS [41], LBF [35], LIF [36], WBHMS [52], ABC [42] and our proposed CTVS model. In general, the segmentation results of the CTVS model are generally consistent with the labeled segmentation results. Furthermore, it is clear from Figure 10 that another segmentation models are not as effective as our proposed CTVS model. In particular, the CTVS model outperforms the others in terms of the treatment of the internal structure.

To quantify the effect of segmentation, we consider the segmentation evaluation as shown in Table 3. It can be seen that the proposed CVTS model gives the highest average of the four measurements among the models used. The results show that the CTVS model is effective in segmenting glioma in some medical images.

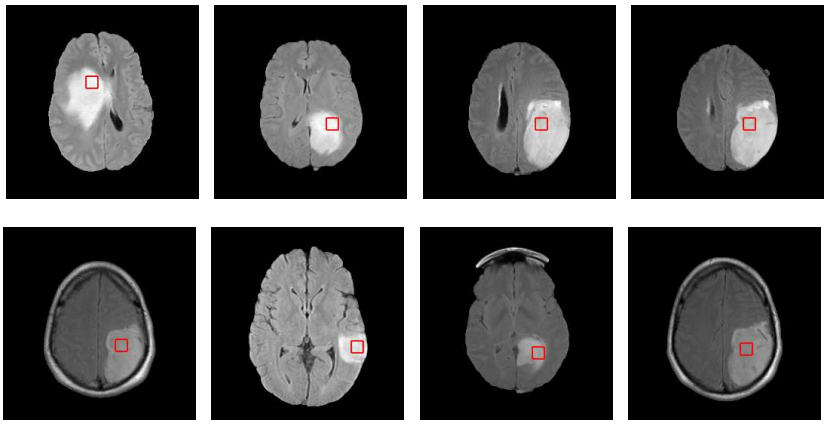


Fig. 9: The results of the skull stripping and initial contour selection.

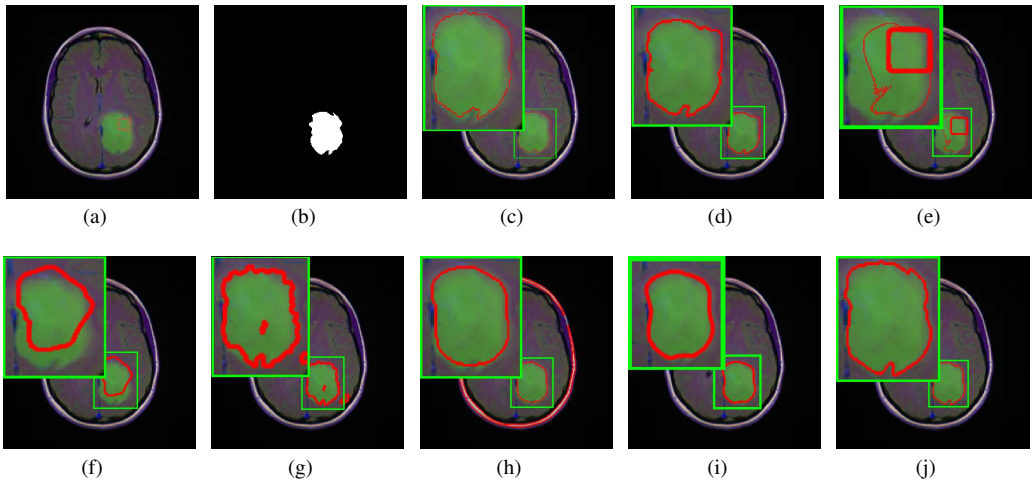


Fig. 10: Segmentation details of different models. (a) Original Image; (b) Ground truth; (c) ICTM; (d) ICTMB; (e) L1PS; (f) LBF; (g) LIF; (h) WBHMS; (i) ABC; (j) CTVS.

5 Conclusion

This paper presented a novel hybrid bias field correction model for segmenting images with intensity inhomogeneity. The model decomposed an image into a piecewise constant component and a smoothly varying bias field. In the proposed model, the bias field constraint was added, which effectively realized the bias field correction and edge information retention of the image. For the numerical method, the proposed model was efficiently solved via an ADM method after variable decoupling. Experimental results show that the proposed model had better robustness and stability than several advanced segmentation models.

Criterions	JS								Accuracy							
Images	ICTM	ICTMB	L1PS	LBF	LIF	WBHMS	ABC	CTVS	ICTM	ICTMB	L1PS	LBF	LIF	WBHMS	ABC	CTVS
M1	0.7871	0.9932	0.7242	0.5176	0.9851	0.9378	0.8384	0.9927	0.9882	0.9875	0.9854	0.9762	0.9856	0.9402	0.9911	0.9930
M2	0.8853	0.9971	0.6200	0.6079	0.9949	0.9706	0.8286	0.9968	0.9962	0.9976	0.9880	0.9871	0.9950	0.9714	0.9939	0.9959
M3	0.7379	0.9850	0.7336	0.6562	0.9856	0.9747	0.4727	0.9959	0.9773	0.9943	0.9772	0.9767	0.9864	0.9761	0.9303	0.9961
M4	0.6837	0.9953	0.8419	0.5878	0.9892	0.9717	0.8065	0.9970	0.9716	0.9956	0.9887	0.9722	0.9898	0.9733	0.9859	0.9950
M5	0.6427	0.9836	0.9115	0.5065	0.9948	0.9691	0.4580	0.9950	0.9758	0.9939	0.9954	0.9739	0.9951	0.9704	0.9423	0.9953
M6	0.8851	0.9871	0.8240	0.7339	0.9945	0.9551	0.7780	0.9971	0.9977	0.9854	0.9963	0.9946	0.9946	0.9559	0.9950	0.9971
M7	0.8175	0.9883	0.3614	0.7063	0.9954	0.9738	0.8799	0.9936	0.9956	0.9876	0.9709	0.9935	0.9955	0.9743	0.9974	0.9938
M8	0.9284	0.9943	0.7497	0.4427	0.9942	0.9763	0.8522	0.9962	0.956	0.9876	0.9810	0.9671	0.9945	0.9774	0.9902	0.9964
Mean	0.7958	0.9905	0.7208	0.5949	0.9917	0.9661	0.7393	**0.9955**	0.9823	0.9912	0.9854	0.9802	0.9921	0.9674	0.9783	**0.9953**
Criterions	F1-score								κ							
Images	ICTM	ICTMB	L1PS	LBF	LIF	WBHMS	ABC	CTVS	ICTM	ICTMB	L1PS	LBF	LIF	WBHMS	ABC	CTVS
M1	0.8809	0.9966	0.8422	0.6822	0.9925	0.9579	0.9121	0.9963	0.8747	0.9233	0.8346	0.6707	0.8195	0.5401	0.9074	0.9410
M2	0.9392	0.9985	0.7654	0.7561	0.9974	0.9851	0.9031	0.9984	0.9372	0.9509	0.7594	0.7496	0.9138	0.6426	0.9031	0.9548
M3	0.8429	0.9975	0.8464	0.7942	0.9928	0.9872	0.6417	0.9979	0.8372	0.9607	0.8343	0.7803	0.8869	0.8181	0.6081	0.9681
M4	0.8122	0.9977	0.9141	0.7404	0.9945	0.9857	0.8929	0.9985	0.7974	0.9609	0.9081	0.7261	0.9123	0 .7923	0.8854	0.9751
M5	0.7825	0.9068	0.9537	0.6724	0.9974	0.9843	0.6282	0.9975	0.7698	0.9301	0.9513	0.6595	0.9478	0.7173	0.6015	0.9472
M6	0.9391	0.9986	0.9035	0.8466	0.9973	0.9771	0.8751	0.9985	0.9379	0.9259	0.9016	0.8438	0.8719	0.4339	0.8726	0.9276
M7	0.8996	0.9991	0.5309	0.8278	0.9977	0.9867	0.9361	0.9968	0.8973	0.9552	0.5178	0.8246	0.8928	0.5726	0.9348	0.9133
M8	0.9629	0.9971	0.8569	0.6137	0.9971	0.9880	0.9202	0.9981	0.9605	0.9488	0.8470	0.5988	0.9502	0.8021	0.9150	0.9664
Mean	0.8824	0.9865	0.8266	0.7417	0.9958	0.9815	0.8387	**0.9978**	0.8765	0.9445	0.8193	0.7317	0.8994	0.6649	0.8285	**0.9492**

Table 3: The index values of the segmentation results of our model and the comparison models in MRI images.

6 Acknowledgements

This work was supported in part by Natural Science Foundation of China (Nos.12471398, 82471962), the Key Scientific Research Projects in Universities in Henan Province (No.24B110004), Henan Province International Science and Technology Cooperation Project (No.242102520038), Medical science and technology research project of Henan province (SBGJ202101013).

7 Data availability statement

Publicly available datasets were analyzed in this study. Access links to the datasets are provided in the main text of the article.

References

1. Xiong X, Wu Z, Tan S, et al. Sam2-unet: Segment anything 2 makes strong encoder for natural and medical image segmentation[J]. Visual Intelligence, 4(1): 2, 2026 .
2. Khan A, Rauf Z, Khan A R, et al. A recent survey of vision transformers for medical image segmentation[J]. IEEE Access, 2025.
3. Rayed M E, Islam S M S, Niha S I, et al. Deep learning for medical image segmentation: State-of-the-art advancements and challenges. Informatics in Medicine Unlocked, 101504, 2024.
4. Kumar A. Study and analysis of different segmentation methods for brain tumor MRI application. Multimedia Tools and Applications, 82(5):7117-7139, 2023.
5. Lin Y, Zhang D, Fang X, et al. Rethinking boundary detection in deep learning models for medical image segmentation. International conference on information processing in medical imaging. Cham: Springer Nature Switzerland, 730-742, 2023.
6. Sun G, Pan Y, Kong. W , et al. DA-TransUNet: integrating spatial and channel dual attention with transformer U-net for medical image segmentation[J]. Frontiers in Bioengineering and Biotechnology, 12:1398237, 2024.
7. Gao Y, Xia W, Hu D, et al. Desam: Decoupled segment anything model for generalizable medical image segmentation. International Conference on Medical Image Computing and Computer-Assisted Intervention. Cham: Springer Nature Switzerland, 509-519, 2024.
8. Zhang Q, Xing G, Zhang J, et al. Adaptive active contours driven by the squared Hellinger distance and local correlation features for inhomogeneous image segmentation[J]. Multimedia Tools and Applications,84(13): 11679-11706, 2025.
9. Hsieh P W, Tseng C L, Yang S Y. Additive-Bias-Correction Variational Model for Noisy and Intensity-Inhomogeneous Image Segmentation[J]. SIAM Journal on Imaging Sciences, 18(2): 1235-1259, 2025.
10. Mumford, David and Jayant Shah. Optimal approximations by piecewise smooth functions and associated variational problems. Communications on Pure and Applied Mathematics 42: 577-685 ,1989.
11. Ullah F, Ullah I, Khan R U, et al. Conventional to deep ensemble methods for hyperspectral image classification: A comprehensive survey. IEEE Journal of Selected Topics in Applied Earth Observations and Remote Sensing, 17:3878-3916, 2024.
12. Wu J, Wang Z, Hong M, et al. Medical sam adapter: Adapting segment anything model for medical image segmentation. Medical image analysis, 102: 103547, 2025.
13. Iqbal S, Khan T M, Naqvi S S, et al. TBConvL-Net: A hybrid deep learning architecture for robust medical image segmentation[J]. Pattern Recognition, 158: 111028, 2025.
14. Trigka M, Dritsas E. A comprehensive survey of deep learning approaches in image processing[J]. Sensors, 25(2): 531, 2025.
15. Xia Q, Zheng H, Zou H, et al. A comprehensive review of deep learning for medical image segmentation[J]. Neurocomputing, 613: 128740, 2025.

16. Wu Q. Research on deep learning image processing technology of second-order partial differential equations. Neural Computing and Applications, 35(3):2183-2195, 2023.
17. Wang D, Wang X P. The iterative convolution–thresholding method (ICTM) for image segmentation. Pattern Recognition, 130: 108794, 2022.
18. Maaliw R R, Mabunga Z P, De Veluz M R D, et al. An enhanced segmentation and deep learning architecture for early diabetic retinopathy detection//2023 IEEE 13th Annual Computing and Communication Workshop and Conference (CCWC). IEEE, 0168-0175, 2023.
19. Pang Z, Guan Z, Li Y, Chen K, et al. Image Segmentation Based on the Hybrid Bias Field Correction. Applied Mathematics and Computation, 452:128050, 2023.
20. Atasever S, Azginoglu N, Terzi D S, et al. A comprehensive survey of deep learning research on medical image analysis with focus on transfer learning. Clinical imaging, 94: 18-41, 2023.
21. Wang H, Jin Q, Li S, et al. A comprehensive survey on deep active learning in medical image analysis. Medical Image Analysis, 103201, 2024.
22. Xie X, Zhang W, Pan X, et al. Canet: Context aware network with dual-stream pyramid for medical image segmentation. Biomedical Signal Processing and Control, 81: 104437, 2023.
23. Chen B, Liu Y, Zhang Z, et al. Transattunet: Multi-level attention-guided u-net with transformer for medical image segmentation. IEEE Transactions on Emerging Topics in Computational Intelligence, 8(1): 55-68, 2023.
24. Ullah F, Nadeem M, Abrar M, et al. Brain tumor segmentation from MRI images using handcrafted convolutional neural network. Diagnostics, 2023, 13(16):2650, 2023.
25. Michael K, Andrew W, and Demetri T. Snakes: Active contour models. International Journal of Computer Vision, 321-331, 1988.
26. Li Z, Zhang F, Wang G, et al. An active contour model based on Kullback–Leibler divergence and morphology for image segmentation with edge leakage[J]. Signal Processing, 238: 110143, 2026.
27. Yang C, Weng G, Chen Y. Active contour model based on local Kullback–Leibler divergence for fast image segmentation. Engineering Applications of Artificial Intelligence, 123:106472, 2023.
28. Li W, Liu W, Zhu J, et al. Box2mask: Box-supervised instance segmentation via level-set evolution. IEEE Transactions on Pattern Analysis and Machine Intelligence, 46(7):5157-5173, 2024.
29. Mitiche A. and Ayed I. B. Variational and Level Set Methods in Image segmentation. Springer Science & Business Media, 2010.
30. Shu X, Yang Y, Liu J, et al. ALVLS: Adaptive local variances-Based levelset framework for medical images segmentation. Pattern Recognition, 136:109257, 2023.
31. Wali S, Li C, Imran M, et al. Level-set evolution for medical image segmentation with alternating direction method of multipliers. Signal Processing, 211:109105, 2023.
32. Preethi P, Mamatha H R. Region-based convolutional neural network for segmenting text in epigraphical images//Artificial Intelligence and Applications, 1(2):103-111, 2023.
33. Li F, Xiang W, Zhang L, et al. Joint optic disk and cup segmentation for glaucoma screening using a region-based deep learning network. Eye, 37(6): 1080-1087, 2023.
34. Yu H, He F, and Pan Y. A novel region-based active contour model via local patch similarity measure for image segmentation. Multimedia Tools and Applications, 77(18):24097-24119, 2018.
35. Li C, Kao C, Gore J, and Ding Z. Implicit Active contours driven by local binary fitting energy. IEEE Transactions on Image Processing, 17(10):1940-1949, 2008.
36. Zhang K, Song H, and Zhang L. Active contours driven by local image fitting energy. Pattern Recognition, 43(4):1199-1206, 2010.
37. Li C, Huang R, Ding Z, Gatenby J, et al. A level set method for image segmentation in the presence of intensity inhomogeneities with application to MRI. IEEE Transactions on Image Processing. 20(7):2007-2016, 2011.
38. Cai Q, Liu H, Zhou S, Sun J, et al. An adaptive-scale active contour model for inhomogeneous image segmentation and bias field estimation. Pattern Recognit. 82:79-93, 2018.
39. Wu Y, Li M, hang Q, and Liu Y. A retinex modulated piecewise constant variational model for image segmentation and bias correction. Applied Mathematical Modelling, 54:697-709, 2017.
40. Vese L and Chan T. A multiphase level set framework for image segmentation using the Mumford and Shah model. International Journal of Computer Vision, 50(3):271-293, 2002.
41. Jung M. Piecewise-smooth image segmentation models with L1 data-fidelity terms. Journal of Scientific Computing, 70:1229-1261, 2017.
42. Weng G, Dong B, and Lei Y. A level set method based on additive bias correction for image segmentation. Expert Systems with Applications, 185:115633, 2021.
43. Dominique Z, Jing A, James S, Nicholas T, et al. Image segmentation with dynamic artifacts detection and bias correction. Inverse Problems and Imaging, 11(3):577-600, 2017.
44. Li C, Gore J, and Davatzikos C. Multiplicative intrinsic component optimization (MICO) for MRI bias field estimation and tissue segmentation. Magnetic Resonance Imaging, 32(7):913-923, 2014.
45. Jin Z, Wu Y, Min L, and Ng M, A retinex-based total variation approach for image segmentation and bias correction, Applied Mathematical Modelling, 79:52-67, 2019.
46. Mishro P.K., Agrawal S., Panda R., Dora L. and Abraham A. Intensity inhomogeneity correction in brain MRI: a systematic review of techniques, current trends and future challenges. Neural Computing and Applications, 1-18, 2024.
47. Huang K., Li Z, Tang S., Zeng Y., Ye W. and Yang F. A level-set method with the 3D multiplicative-additive model for CT volume data segmentation. Measurement, 229:114442, 2024.
48. Shu X, Li Z, Chang X, and Yuan D. Variational methods with application to medical image segmentation: A survey. Neurocomputing, 9:130260, 2025.
49. Zhang H, Lu P, Qi T, et al. Adaptive Superpixel-Guided Non-Homogeneous Image Dehazing[J]. IEEE Signal Processing Letters, 2025.
50. Cao J, Chen, K, and Han H. A fractional-order image segmentation model with application to low-contrast and piecewise smooth images. Computers & Mathematics with Applications, 153:159-171, 2024

51. Zhang, Q, Xing, G, Zhang, J. et al. Adaptive active contours driven by the squared Hellinger distance and local correlation features for inhomogeneous image segmentation. Multimedia Tools and Applications, 84:11679–11706, 2025.
52. Yang Y, Zhong Q, Duan Y, and Zeng T. A weighted bounded hessian variational model for image labeling and segmentation. Signal Processing, 173:107564, 2020.